ORIGINAL RESEARCH ARTICLE

# Investigation on the Microstructure Evolution and Properties of a Novel In-Situ Fiber Phase-Reinforced Nickel Composite Coating Deposited by Wide-Band Laser

Xing Wang[1] · Nannan Ren[1] · Kun Zhao[1] · Wei Meng[1] · Hu Xie[1] · Xiaohui Yin[1] · Qunshuang Ma[1,2]

**Abstract** In this paper, a novel hard nickel composite coatings were fabricated by wide-band laser cladding technique. The effects of Si alloying on the composite coatings were investigated by microstructure characterization, phase identification, microhardness and wear resistance. Results showed that the in-situ precipitated phases in the laser molten pool were composed of the $\gamma$-Ni solid solution and hard phases such as $Cr_{23}C_6$, $CrSi$, $Cr_5B_3$. With the increase of Si element, the morphology of the precipitated phases changed significantly. When the added content of Si was 1.0 wt.%, the precipitated phase was a mainly block morphology. As the added content of Si was increased to more than 2.0 wt.%, the main precipitated phase was transformed into a long stripe morphology. With the increase of Si content, the stripe-like precipitated phase was gradually refined and finally becomes density needle-like precipitates. Element distribution analysis showed that the block precipitated phase was enriched in Cr, W and Si elements. Additionally, the enriched elements in the long strip precipitation phase were essentially the same as those in the block precipitation phase. The added Si element was highly involved in the in-situ reactions of precipitated phase. The TEM results showed that the precipitated phases contained the crystal structures of $Cr_5B_3$ and $Cr_7C_3$. The pin-on-disc wear tests revealed that the composite coating with the addition of 6 wt.% Si exhibited the best wear resistance in the experimental group. The average friction coefficient was about 0.6 and the wear mass loss rate was about $2.38 \times 10^{-5}$ g/m under counter-abrasive conditions. The worn surface analysis indicated that the wear mechanism of composite coatings was mainly abrasive wear. The refined needle-like precipitated phase was closely bound to the matrix and thus not easy to peel off, providing a significant improvement in the wear resistance of the laser cladding coatings.

**Keywords** alloying effect · nickel-based coatings · reinforced phases · wide-band laser cladding · wear resistance

## 1. Introduction

As a surface modification technique, laser cladding has the potential to enhance the wear and corrosion resistance of low-cost carbon steel. This is achieved by applying high-performance composite coatings to the surface of conventional carbon steel (Ref 1-3). It is worth noting that laser cladding can be utilized to alter the surface properties of numerous materials. In contrast to conventional surface modification methods, laser cladding exhibits robust metallurgical bonding, high cladding quality and minimal substrate distortion. Thus, it has been extensively used in the various area of industrial production, such as mechanical engineering, mold repair and military weaponry (Ref 4, 5). As is known, metal matrix ceramic composites (MMCs) are composed of metal matrix phase and hard ceramic reinforcement phase. The metal matrix phase

✉ Nannan Ren
nnren@ahut.edu.cn

✉ Qunshuang Ma
maqunshuang@126.com

1   School of Materials Science and Engineering, Anhui University of Technology, Maanshan 243032, People's Republic of China

2   Key Laboratory of Green Fabrication and Surface Technology of Advanced Metal Materials (Anhui University of Technology), Ministry of Education, Maanshan 243002, People's Republic of China

🌀 Springer

has low hardness and good toughness, while the dispersive ceramic phase has high hardness. These reinforced phases generated by in-situ reaction are tightly combined with the matrix phase, which can highly improve the wear resistance of the composite coating (Ref 6-8). Typically, metal powders such as Ni (Ref 9, 10), Fe (Ref 11, 12), Zr (Ref 13, 14) and Mo (Ref 15) could be used as cladding materials. Among them, the Ni-based alloy powders are often used as cladding materials to improve the wear resistance of low-cost carbon steel surfaces due to their good wettability and self-solubility (Ref 16). To further improve the performance of the nickel-based cladding layers, researchers have tried to induce the hard ceramic particles like WC, TiC into laser molten pool (Ref 17, 18). It is reported that the addition of hard ceramic particles could significantly increase the hardness and wear resistance of the cladding laser. However, the extra-added ceramic particles are usually non-uniform distributed in the composite coating layer, which led to the toughness decrease and cracks initiation (Ref 19).

In order to improve the deficiency of extra-added reinforced particles, various elements were added by the alloying method to promote the in-situ synthesis of reinforced phase in laser molten pool. This way of introducing the reinforcement phase can significantly improve the distribution, morphology and density of reinforcement phase, so as to obtain better reinforcement effect (Ref 20-22). Gao et al investigated the influence of Fe content on the phase and properties of nickel-based composite coatings (Ref 23). The result showed that the Fe element transformed the ternary eutectic phase in the melt-coated layer into a γ-FCC/ (Cr, Fe)7C3 eutectic phase. The disappearance of the hard phase in the coating and the uniformity of the Cr distribution in the coating were also observed. When the iron content reached 25%, the composite coating exhibited superior corrosion and wear resistance. Li studied the effect of chromium content on the microstructure and wear resistance of titanium-based coatings (Ref 24). Under high-temperature friction conditions, the addition of Cr resulted in the formation of a superhard amorphous oxide protective layer on the worn surface, which improved the wear resistance of the coating. Hong et al investigated the effect of Nb additions on the in-situ precipitation reinforced phase and wear resistance of the composite coatings with respect to the Nb element (Ref 25). The results showed that when the Nb content reached 3 wt.%, the needle-like agglomerates of NbC phases had the best wear resistance properties. Liang et al found that the addition of rare earth oxide resulted in the coating layer without obvious pores, cracks and delamination, where the internal distribution of the grains is more regular and the microstructure is more refined (Ref 26). Through the above studies, it is revealed that the elements added in the laser molten pool are dissolved in large quantities under the proper laser irradiation energy. These elements with strong carbide-forming ability such as Cr, Nb, Fe could highly involve in the in-situ reactions to form newly precipitated in-situ hard phases in the melting pool. Compared with the externally applied WC reinforced phases, the new precipitated phases in the cladding layers are significantly different in their morphology and grain size. These reinforced phases have better improvement effects on the microhardness and wear resistance of the cladding layer.

In the alloying research of laser molten pool, modulation of the in-situ reaction by precursor element is a widely used method. For composite coatings reinforced with carbide precipitation phases, the in-situ synthesis path of the reinforcing phases can also be regulated by changing the form and concentration of the C element in the precursor material or in the melt pool. For example, Li et al utilized the DED method to incorporate carbon nanotubes into Ni60/WC powders resulting in a refined microstructure (Ref 27). Furthermore, the addition of carbon nanotubes in the composite coatings led to a significant increase in the microhardness and wear resistance. Yuan et al applied a composite coating consisting of FeCrAl/TiC to the surface of ferritic steel (Ref 28). The results show that the addition of TiC is capable of refining the grains, changing the morphology from columnar to equiaxed and avoiding cracking in the coating. This improves the wear resistance of the composite coating. Ning et al created composite coatings by incorporating SiC into the nickel-based alloy powders (Ref 29). The addition of SiC ceramic particles refined the microstructure, and the metal carbide that resulted from SiC decomposition combined with diffusion elements in the matrix to enhance the microhardness of the cladding layer. As the content of SiC increased, wear resistance of the coatings also significantly improved. Singh et al fabricated a powder coating made of NiCr-SiBC + 50WC on SS410 steel and examined the impacts of laser beam power, scanning speed and powder feeding rate on the quality of fusion coating (Ref 30). As a result, elevated laser power caused the metal and coating powder to melt, leading to grain refinement. Higher laser power needs to be combined with higher scanning speed and moderate powder feeding rate to accomplish the superior quality of coatings.

In most nickel-based laser cladding materials, a certain amount of Si element can promote the formation of silicate oxide slag to protect the high-temperature molten pool. However, there has been very limited reporting on the role of added Si element in the in-situ reactions of the melt pool. Liang et al prepared a composite coating with added Si on a titanium alloy substrate and found that the addition of Si in the cladding layer resulted in the formation of an enhanced Ti5Si3 phase and a Ti5Si3-Ti2Ni eutectic

structure (Ref 31). These structures became intimately coupled to the matrix phase, thereby greatly improving the strength and toughness of the fusion clad. Zhu et al. investigated the effect of Cu/Si on the wear resistance of high-entropy alloys, and the results showed that the addition of Si elements refined the grain size and improved the wear resistance of the coating (Ref 32). The above reports on the role of Si concentrates on its effect on the grain structure of the fusion cladding substrate, particularly in refining the grain size and improving the bonding between the matrix phase and the eutectic structure. Further investigation is required to determine whether the in-situ addition of Si is involved in the reaction for nickel-based coatings reinforced by in-situ precipitated phases and how this affects the nucleation, growth and final morphology of the precipitated phases.

Based on the aforementioned study, this work incorporates silicon (Si) element to the precursor material utilized in laser cladding. Subsequently, a wide-band laser is employed to dissolve the additional precursor materials in the melt pool and induce the in-situ reactions of hard ceramic particles. This research explores whether the in-situ reaction between Si element and the enriched elements found in the melt pool, yields benefit in terms of achieving greater refinement in the microstructure of the cladding layer and improving the homogeneity of precipitated phases. The ultimate objective of this work is to enhance the microhardness and abrasion resistance of the laser clad layers.

## 2. Materials and Methods

The substrate chosen for laser cladding was Q550 low-alloy high-tensile steel, characterized by 10 mm thickness. The composition and mechanical properties of this steel were detailed in former reference (Ref 33). The specimen was precisely cut from the base steel with dimensions of $10 \times 20 \times 100mm^3$, using a wire cutting equipment. Prior to laser cladding, the oxide surface layer of the base steel was meticulously removed through grinding and subsequently cleaned with alcohol. The laser cladding material is a mixture of commercial Ni60 self-fluxing alloy powder, WC powder and Si powder. The chemical composition of the Ni60 alloy powder is characterized by 0.85% C, 3.60% B, 14.00% Cr, 16.00% Fe, 4.50% Si and 61.05% Ni in weight percentage. The designed composition of the different cladding layer is outlined in Table 1. The SEM morphology and particle size distribution of the added powders are depicted in Fig. 1. The Ni60 powder exhibits a standard spherical shape with uniform particle size (D50 = 73.34 µm). In contrast, the WC powder displays polygonal particles with a coarser particle size

**Table 1** Composition design of different composite coatings (wt.%).

| No. | Commercial Ni60 powder | WC powder | Si powder |
|-----|------------------------|-----------|-----------|
| 0#  | 80                     | 20        | 0         |
| 1#  | 79                     | 20        | 1         |
| 2#  | 78                     | 20        | 2         |
| 3#  | 76                     | 20        | 4         |
| 4#  | 74                     | 20        | 6         |

(D50 = 86.79 µm). Meanwhile, the Si powder features smaller particles with uniform distribution (D50 = 9.25 µm).

A powder layer with approximately 1.0 mm in thickness was meticulously prepared on the surface of the base steel using alcohol. Following the completion of the prepared powder process, the specimens underwent a drying process. To eliminate any residual moisture from the powder layer, the samples were heated to 150 °C and held for 30 minutes before the laser cladding. A fiber-coupled semiconductor laser (Laserline LDF4000-100, Germany) was applied in laser cladding process. The dimensions of wide-band laser spot employed in these experiments were 15 mm × 2 mm. Optimized laser processing parameters included a laser power of 3.0 kW, scanning speed of 3.0 mm/s, laser head focal length of 150 mm and a defocusing distance of 0 mm. Throughout the laser cladding process, a shielding gas consisting of pure 99.9% Ar was directed flow into the melt pool at a flow rate of 15 L/min to prevent high-temperature oxidation. Upon completion, the samples were cooled spontaneously to room temperature in the air atmosphere.

Following the laser cladding process, the metallographic and XRD test specimens were sliced along the cross section using a wire cutting machine. To examine the coating microstructure, the metallographic specimens underwent a polishing process using 160-1000# SiC grit paper, followed by corrosion process using a mixture acid of 20% HF, 30% HCl and 50% $HNO_3$ at room temperature (20 °C) for 10 seconds. Microstructures were meticulously observed utilizing an XJP-6A optical microscope and a scanning electron microscope (SEM, JSM-6490LV). Elemental analysis of the microstructure was conducted using an energy spectrometer (EDS, Oxford X-Max 50). Additionally, the phase microstructure of various cladding layers was scrutinized using an x-ray diffractometer (XRD, D8ADVANCE). The precipitated phases were further investigated using high-resolution transmission electron microscopy (HR-TEM, JEM2100) for a detailed determination of their crystal structure.

To explore the influence of Si addition on the properties of cladding layers, a digital Vickers microhardness tester
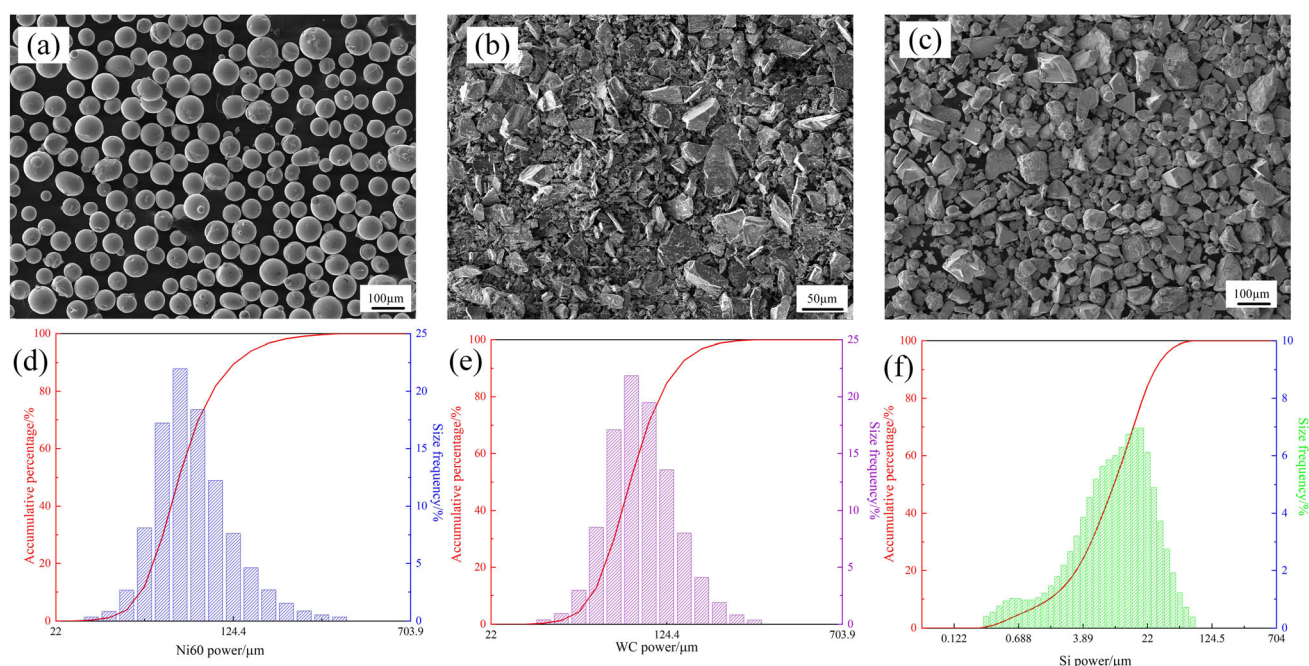
Fig. 1 The morphologies and statistical analysis of laser-deposited materials and size distribution (a-d):Ni60,(b-e):WC,(c-f):Si

was employed for assessing the microhardness of various cladding layers. The microhardness test utilized an HV-1000TPTA hardness tester with a test load of 4.903 N and an indentation dwell time of 10 s. Microhardness measurements were obtained at five points in the substrate section of each specimen and ten points in the cladding layers section, incrementing by 100 μm for each distance from the interface. Additionally, the pin-on-disc wear test was conducted to evaluate the wear resistance of cladding layers. For the pin-on-disc wear test, a cylindrical pin specimen with a diameter of 4 mm was extracted from the cladding layer and subjected to friction and wear perpendicular to the interface direction. The wear test was carried out at room temperature using an MMU-10G wear tester. The friction pair featured a W18Cr4V HSS disc with a diameter of 50 mm, rotating at a velocity of 200 r/min. The microhardness of the disc was 815 HV, and a load of 100 N was applied for 60 minutes to assess the extent of wear.

## Results and Discussion

### Microstructure Analysis

The macroscopic morphology of the wide-band laser clad specimens, following the addition of 1 wt.% Si, 2 wt.% Si, 4 wt.% Si and 6 wt.% Si, is illustrated from left to right in Fig. 2(a). The composite coatings with different Si content exhibited a uniform, smooth and continuous surface, indicating the well forming ability of the designed precursor

powders. The presence of a white lumpy particulate phase at the bottom of the cladding layer is observed in Fig. 2(b), (c) and (d). Previous studies have clarified that the white particle consists of externally added tungsten carbide particles (Ref 34). They are deposited at the bottom of the fused cladding layer due to gravitational forces. With the introduction of silicon, there is minimal variation in the quantity of undissolved white tungsten carbide particles within the composite coatings (Ref 35). However, the size of the externally added WC particles decreased, indicating that the addition of Si facilitates the dissolution of WC.

Figure 3 illustrates the morphology of the cladding microstructure manifested at 500 times under an optical microscope. With an increasing Si concentration, the morphology of the in-situ precipitated reinforced phase undergoes significant changes. Adding with 1 wt.% Si, the precipitates in coating 1# exhibit a block morphology, leading to the formation of a continuous dendritic microstructural distribution, suggesting a certain degree of preferential orientation for the direction of precipitate phase. As the silicon content rises to 2 wt.%, the morphology of the precipitated phase transforms into a thicker stripe shape. As depicted in Fig. 3(c) and (d), the precipitated phase transformed into finer needle-like shape with no discernible direction of growth. Furthermore, the nucleation density of the precipitated phase increases with higher Si content.

In order to further study the effect of Si addition on the in-situ precipitated reinforced phase, SEM was employed to analyze the morphology and elemental composition of

**Fig. 2** Macroscopic observation and microstructure of wide-band laser-deposited nickel composite coating: (a) surface morphology; (b) 0 wt.% Si; (c) 2 wt.% Si:(d) 6 wt.% Si
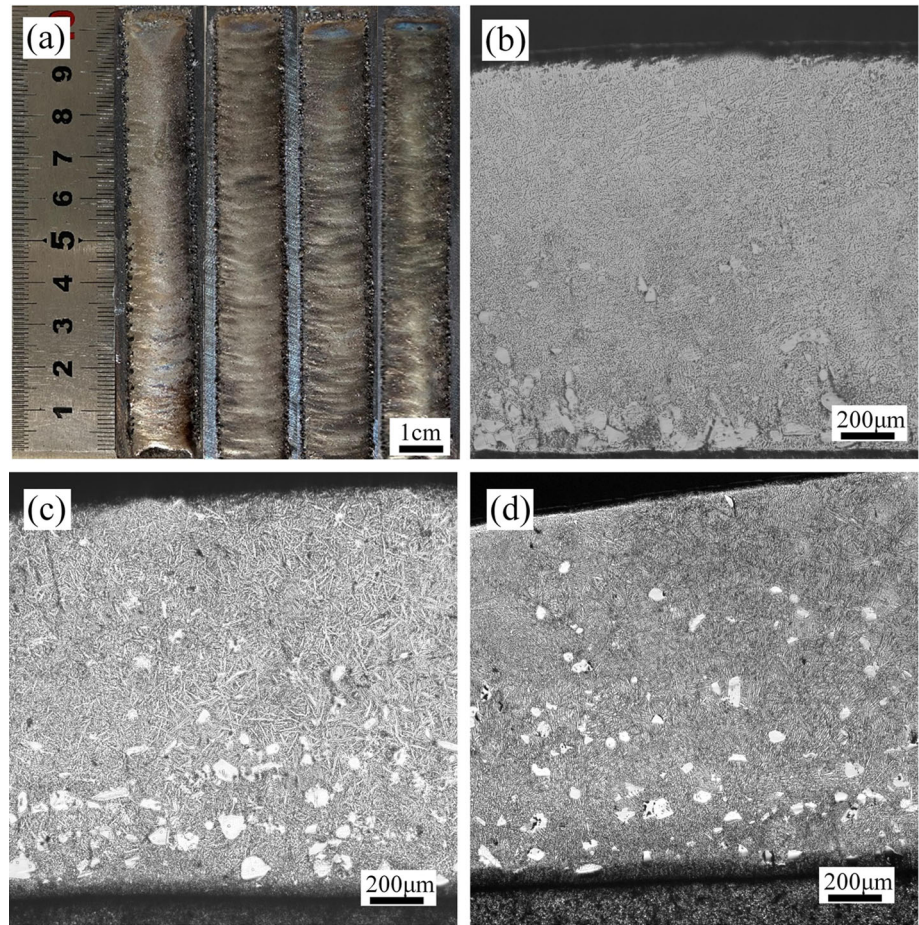


precipitated phases. The findings are presented in Fig. 4. Figure 4(a1) illustrates that the cladding layer with 1 wt.% Si displays a relatively regular morphology of the in-situ precipitated phases. The precipitated phases manifest as block, crosses and tetragonal forms with a preferred orientation. Additionally, a substantial quantity of fine eutectic precipitates is dispersed within the matrix phases. The EDS point composition analysis regarding the precipitated phase in Fig. 4(a2) is detailed in Table 2. The block phase is notably enriched in Cr, W and C elements, along with a certain amount of Si elements. With increase of the Si content in coating 2#, a significant transformation in the morphology of the precipitated phase could be observed. As depicted in Fig. 4(b1), the precipitated phase showed more uniformly striped shape. However, the distribution of striped phases remains relatively disordered, and no apparent growth direction is observed. Figure 4(b2) presents a magnified view of the local microstructure, revealing a bright white area encompassing the stripe-like precipitation phases. Furthermore, the interior exhibits an extremely fine precipitate microstructure consistent with the lamellar eutectic structure. Surrounding the eutectic structure and strip precipitation phase is the nickel matrix.

An examination of the strip precipitate phase through EDS point composition in Table 2 indicates a dominant presence of Cr, W and C with a minor amount of Si elements. It is noteworthy that the W content is significantly higher than that in the precipitated phase shown in Fig. 4(a2).

The morphology of the precipitated phase in the clad layer with 4% Si addition is illustrated in Fig. 4(c1). As shown, the morphology undergoes a transformation from the original coarse striped shape to fine striped shape, also exhibiting irregular growth directions. In comparison with Fig. 4(b1), a decreasing trend in the area of the white eutectic structure surrounding the in-situ precipitated phase can be founded in Fig. 4(c1). The white area of eutectic structure gradually diminishes, while the gray area in the matrix phase remains unchanged. Simultaneously, the density of the in-situ precipitated phase gradually increases. Further analysis of the elemental distribution of the in-situ precipitated reinforced phase is presented in Fig. 4(c2), and the results are detailed in Table 2. The precipitated phase in the coating 3# predominantly consists of Cr, W and a small amount of C elements, with no presence of silicon. Upon increasing the Si element to 6 wt.%, Fig. 4(d1) demonstrates that the morphology of the in-situ

Fig. 3 Microstructures of in-situ precipitated phases in cladding layers with different Si addition: (a) 1 wt.% Si; (b) 2 wt.% Si; (c) 4 wt.% Si; (d) 6 wt.% Si
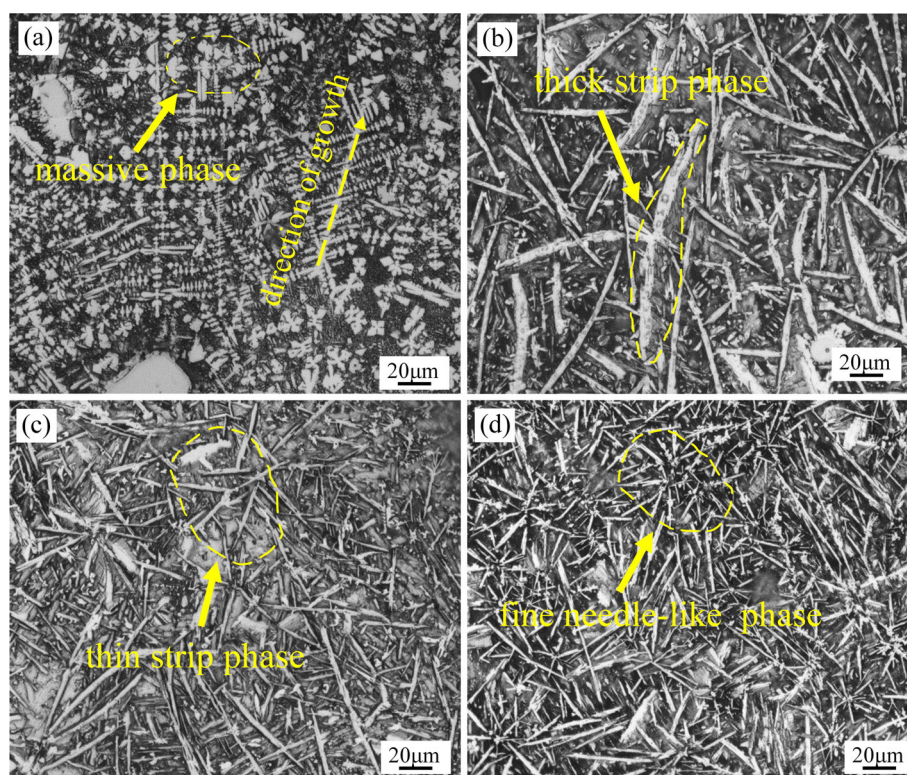


precipitation reinforced phase transforms into fine needle-like microstructures. The precipitated phase is distributed randomly, lacking an apparent pattern of growth direction. In particular, there is no white eutectic structure area around the fine needle-like precipitated phase, and only the gray matrix area is observable in the local magnification area of Fig. 4(d2). Additionally, the density of the precipitated phase tends to increase, eventually partially covering the matrix phase with the rise in Si element content. Conducting an EDS point composition analysis of the precipitated phase in the coating 4# (as detailed in Table 2), it is observed that the precipitated phase primarily comprises Cr, W and C elements, along with a small amount of B elements. This composition closely resembles that of the coating 3#, which lacks Si elements.

## XRD Analysis of Phase Composition

X-ray diffraction (XRD) analyses were conducted to explore the influence of Si element incorporation on the phase composition of the cladding layers. Figure 5(a) displays the results of the control test conducted without the addition of Si. The findings reveal that the cladding layer predominantly consists of a $\gamma$-Ni (Fe) solid solution phase and chromium compounds, specifically $Cr_{23}C_6$ and $Cr_5B_3$. The addition of Si to the cladding layer results in the formation of Si compounds, such as $Ni_{31}Si_{12}$, CrSi and SiC. Given that the base powder of the cladding layer primarily comprises Ni-based self-fusing alloy powder, the intensity of $\gamma$-Ni (Fe) in the composite coating is elevated, with diffraction peaks at 43.6° for the (1 1 1) crystalline plane, 50.8° for the (2 0 0) crystalline plane and 74.7° for the (2 2 0) crystalline diffraction peaks. Upon the addition of WC, which undergoes partial dissolution in the high-temperature laser molten pool, the free C element combines with the Cr element in the molten pool, resulting in the formation of the precipitated phase of $Cr_{23}C_6$. Consequently, the intensity of the diffraction peaks associated with $Cr_{23}C_6$ phase is heightened (Ref 36). However, CrSi exhibits greater stability than carbides. In the presence of free Si in laser molten pool, some of the C elements in chromium carbides are replaced by Si elements (Ref 37).

Notably, some undissolved WC is present in laser molten pool, and due to its higher density, it is deposited in the lower part of the molten cladding layer under gravity. WC diffraction peaks of a certain intensity are also observable in the XRD diffraction peaks. According to the XRD results, the diffraction peak intensity of $Cr_{23}C_6$ gradually decreases with the increase of Si element, while the diffraction peak intensities of $Cr_5B_3$, NiSi, $Ni_{31}Si_{12}$ and other phases exhibit a gradual increase. The composition of phases in the composite coatings remained consistent with the increasing Si element. However, the relative content of precipitated phases, as identified by the intensity of the diffraction peaks, exhibited variations among different coatings. Examination of diffraction peaks at 45.80° and

**Fig. 4** Morphology of in-situ precipitated phases in different coatings: (a1, a2) coating1#; (b1, b2) coating2#; (c1, c2) coating3#; (d1, d2) coating4#
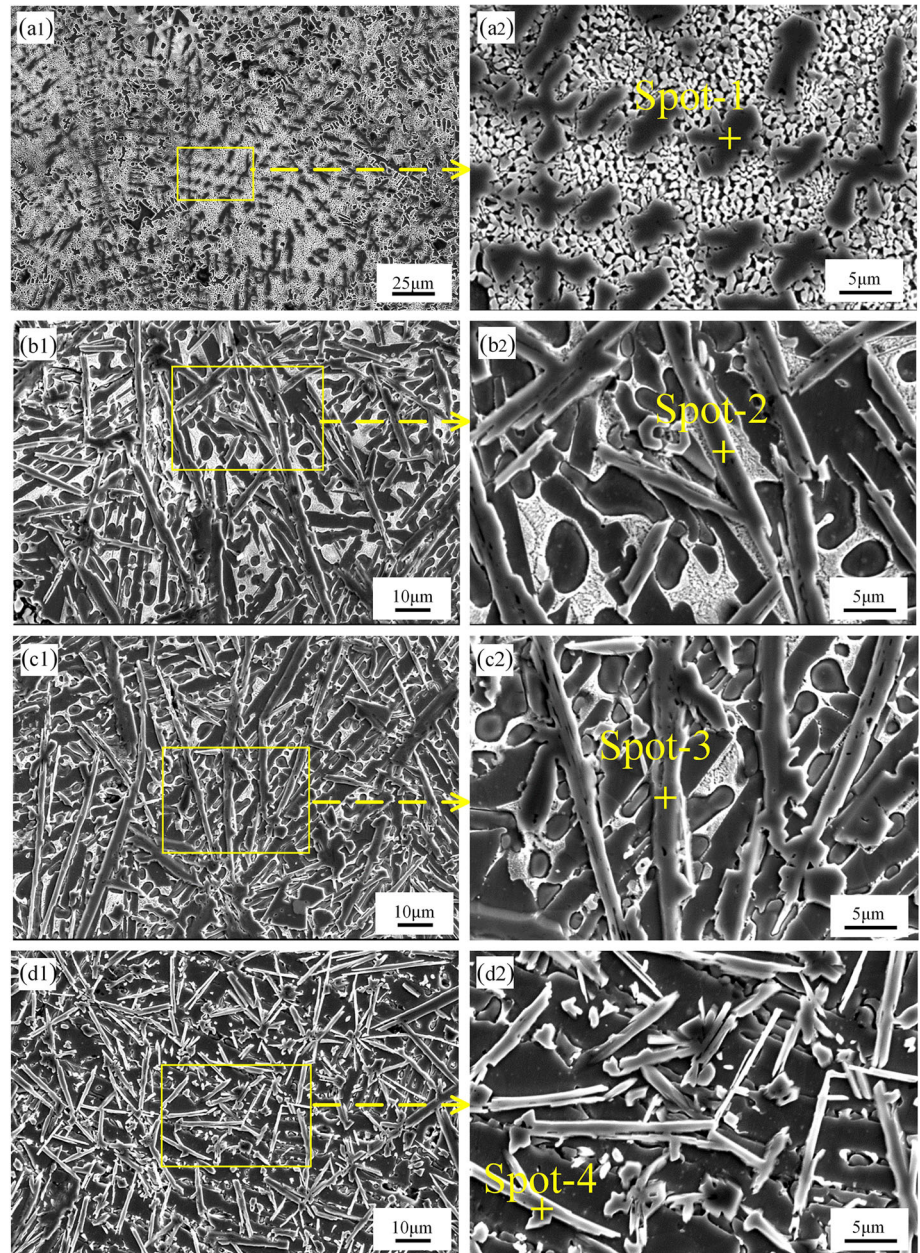


**Table 2** Elemental distribution of in-situ precipitated phases in different cladding layers

| Spot | Element | C | Si | Cr | Fe | Ni | W | B |
|------|---------|------|------|-------|------|-------|-------|-------|
| Spectrum1 | wt.% | 10.34 | 5.28 | 28.24 | 2.62 | 27.72 | 25.80 | … |
| Spectrum2 | wt.% | 7.11 | 1.58 | 34.51 | 1.61 | 13.82 | 41.38 | … |
| Spectrum3 | wt.% | 10.14 | … | 31.63 | 1.10 | 11.85 | 45.29 | … |
| Spectrum4 | wt.% | 11.73 | … | 33.04 | 0.84 | 5.04 | 35.73 | 13.62 |

47.12° reveals a gradual increase in the intensity of diffraction peaks associated with $Cr_5B_3$, NiSi and $Ni_{31}Si_{12}$. This suggests that the augmentation of Si element not only facilitates the formation of Si-containing compounds but also enhances the enrichment of $Cr_5B_3$. The heightened Si element content promotes the interaction between Cr and B

elements in chromides, leading to an increase in the diffraction peak intensity of $Cr_5B_3$. Moreover, diffraction peaks of a certain intensity corresponding to the $W_5(Si, B)_3$ phase were also calibrated in the cladding layer. According to the PDF standard diffraction chart information, $Cr_5B_3$ and $W_5(Si, B)_3$ phases share the same crystal structure type
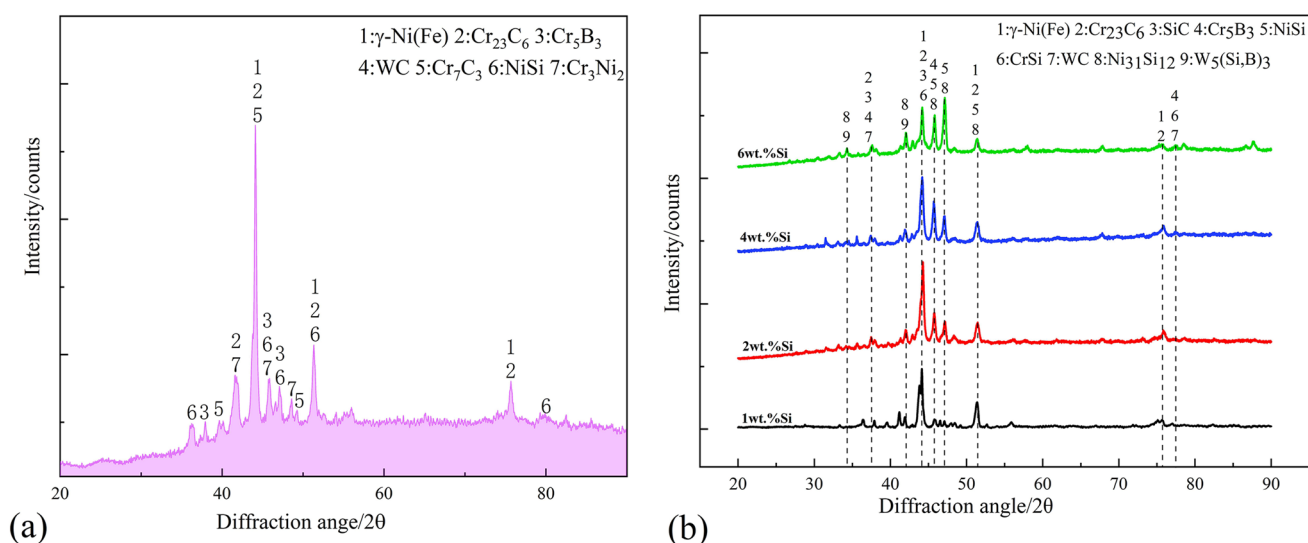
**Fig. 5** Phase composition in different cladding layers by X-ray diffraction examination (a) control group, (b) experimental group

with space group I4/mcm (140) and Pearson symbol tI32. These compounds belong to the $A_5B_3$ type, where the A element position can be occupied by elements like Cr, W and the B position can be occupied by elements such as Si and B.

## Elemental Distribution

During the analysis of in-situ precipitation phases, a notable transformation in the morphology of the precipitated phases was observed. With an increase in Si addition, the in-situ phases transformed from the typical block shape into strip and needle-like shape. To explore the elemental distribution within these diverse morphologies of the precipitated phase, EDS map scanning analysis was conducted. Figure 6 displays the result of the elemental map scanning analysis, focusing on the block precipitated phase situated in the coating 1#. As the microstructure showed, the precipitated phase exhibited a regular block morphology. This hard phase is notably enriched in Si and Cr elements, with minimal presence of Ni and Fe elements. Additionally, W elements show a slight enrichment compared to the surrounding matrix phases. Corroborating with XRD data, this implies that the $(Cr, W)_5(Si, B)_3$ phase predominates as the primary precipitation phases in the coating 1#, manifesting in a block microstructure.

Figure 7 illustrates the results of the EDS map scanning, focusing on the strip precipitated phase in the coating 3#. The results reveal a significantly enrichment of Si and Cr elements in the strip precipitated phase in coating 3# and the deficiency in Ni and Fe elements. Additionally, the W element exhibits higher abundance in the strip precipitated phase compared to the surrounding matrix phase, attributed to the substitution of W for Cr in the chromium

compounds. The primary composition of the precipitated phase in the coating 3# is further suggested to be $(Cr, W)_5(Si, B)_3$, supported by experimental findings from both point and surface scans as well as XRD data. Particularly, elemental analyses confirm a significant involvement of Si in the in-situ synthesis reaction of $A_5B_3$ type compounds with an increasing Si addition. The crystal structure of the precipitated primary phase remains unchanged, but there is a notable morphological transition from a massive to a long strip microstructure.

EDS line scanning was also conducted to validate elemental distribution of the precipitated phase in the cladding layers. The scanning line traversed the block precipitated phase in coating 1# with the addition of 1 wt.% Si, and the results are shown in Fig. 8(a-a7), respectively. The intensity of Si, Cr and W elements exhibits a sudden increase in the central region, while the intensity of Fe and Ni elements diminishes in the same area. This central region aligns with the block precipitation phase depicted in Fig. 8(a), implying that Si, Cr and W have been concentrated in the block precipitation. The EDS scanning line traversed across the long strip precipitation phases as depicted in Fig. 8(b). The elemental distribution results for the composite coating with 4 wt.% Si addition are vividly illustrated in Fig. 8(b1-b7). Notably, three distinct peaks in intensity emerged for the elements Si, B, Cr and W. Impressively, the identified locations of element enrichment zones consistently align with the distribution regions of the long strip precipitate phases showcased in Fig. 8(b). Significantly reduced signal intensities were observed for Fe and Ni elements within the long strip precipitates. This decline suggests a lack of these elements within the block precipitated phases. Moreover, the findings derived from the EDS elemental distribution line scanning validate those
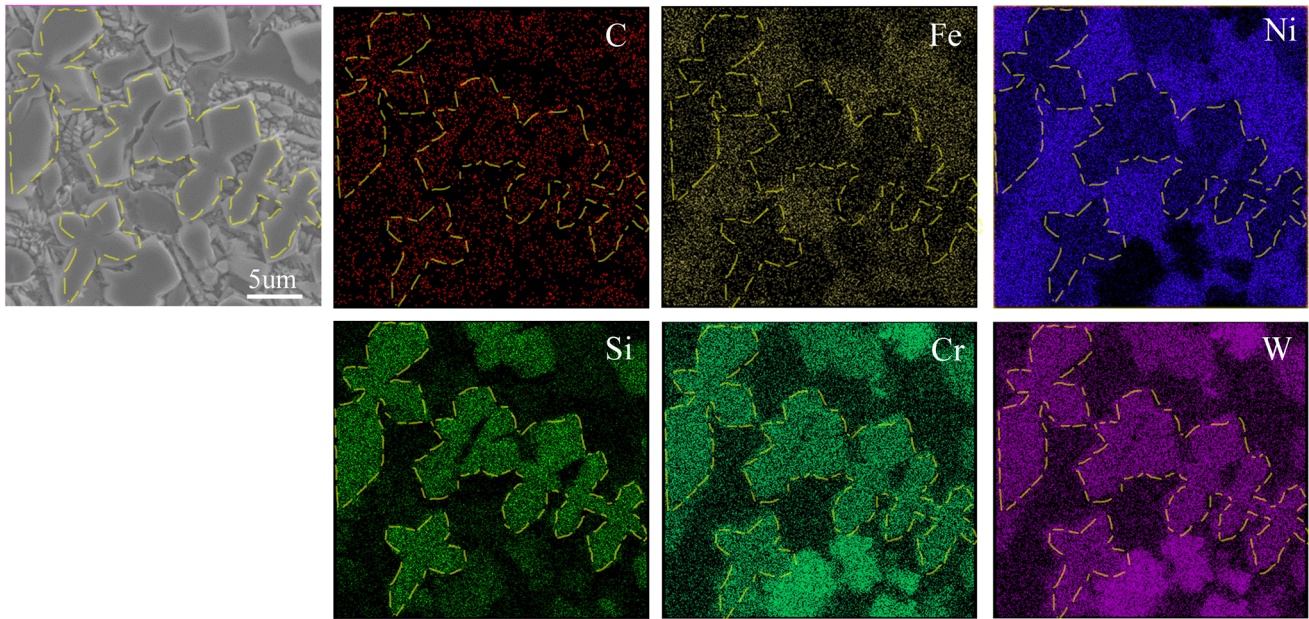
**Fig. 6** Elemental distribution of in-situ precipitated phases in coating 1# with 1 wt.% Si addition
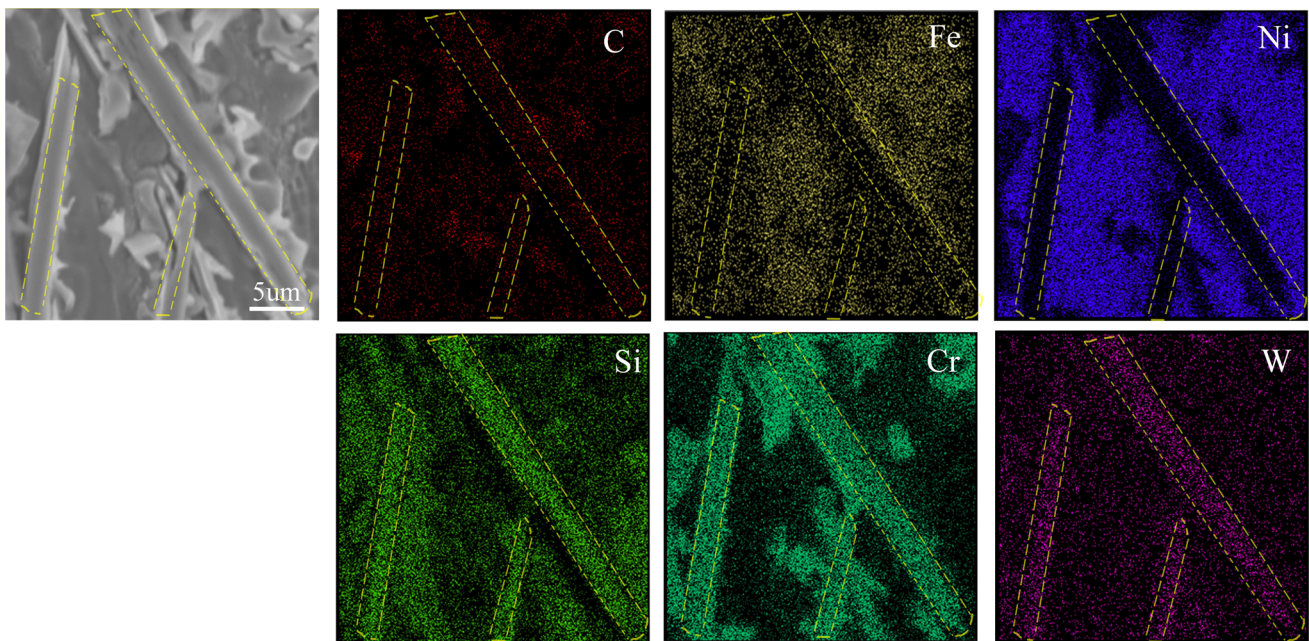


**Fig. 7** Elemental distribution of in-situ precipitated phases in coating 4# with 6wt.% Si addition

of the map scanning. They jointly confirm the enrichment areas for Si, Cr and W elements within the block and strip precipitate phases. However, a striking concentration of B elements is discernible in these long strip precipitate phases. Both XRD and EDS elemental distribution analyses unequivocally establish that the block and long strip precipitates within the claddings 1# and 3# exclusively comprise $(Cr, W)_5(Si, B)_3$ phases. These analyses also suggest that although the crystal structure of the precipitates

remains unchanged, the morphology of primary precipitates within the cladding layers undergoes a transition from the block to the long strip morphology with the increasing of Si content.

**TEM Characterization of In-Situ Precipitated Phase**

TEM characterization was employed to scrutinize the microstructure of the in-situ precipitated phase in the
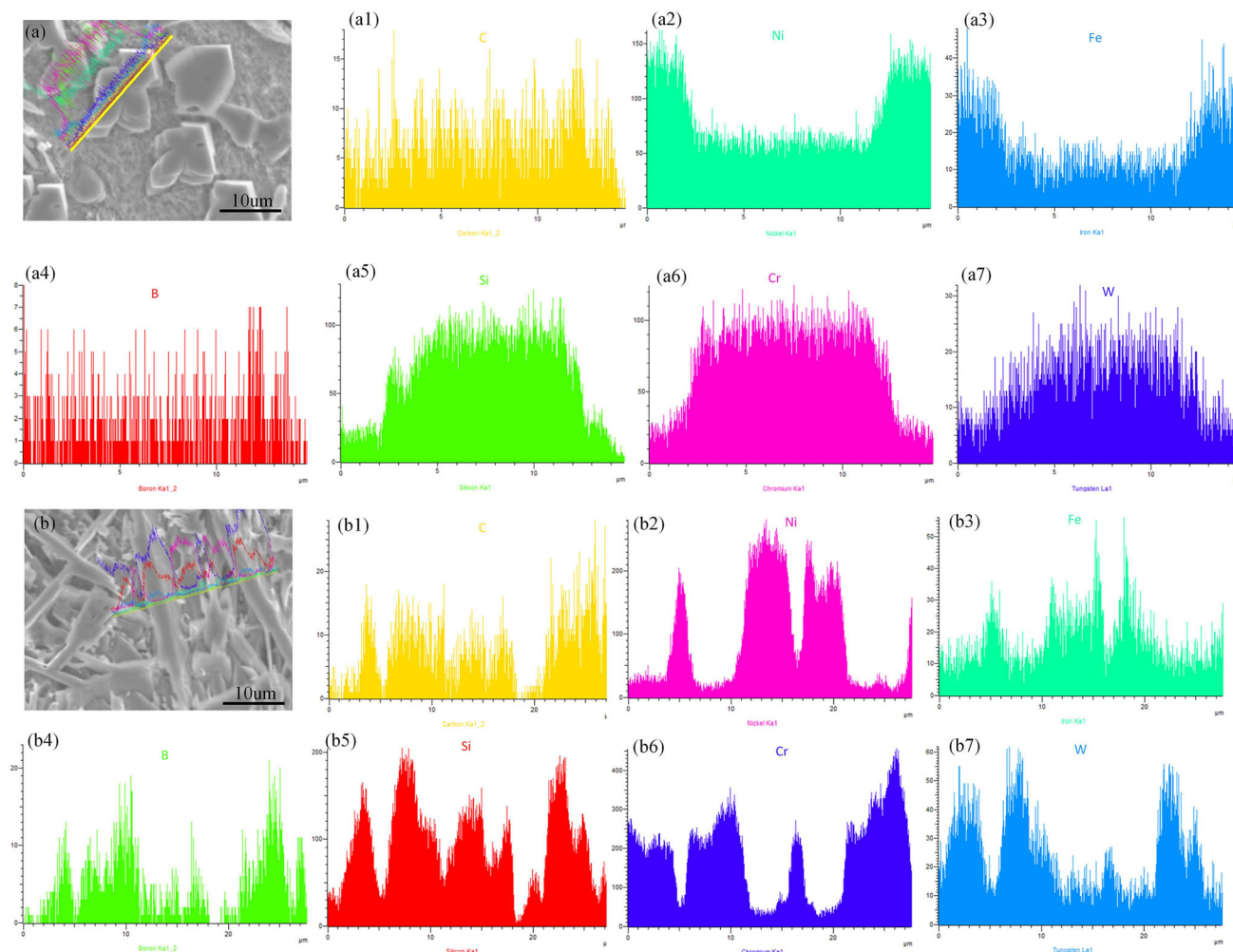
**Fig. 8** (a) Elemental distribution line scanning of block precipitated phases in coating 1#. (b) Elemental distribution line scanning of stripe precipitated phases in coating 3#

4wt.% Si cladding layer. The results are presented in Fig. 8. In Fig. 9(a) and (b), the morphology of the in-situ reinforced phase within the cladding layer is depicted through the bright field image. The image reveals that the matrix γ-Ni phase appears light-colored, and precipitated phases with darker image contrast are discernible. The high-resolution transmission electron microscope micrograph is showed in Fig. 9(d). The selected area diffraction patterns obtained through Fourier transform are illustrated in Fig. 9(c). This phase was conclusively identified as $Cr_{23}C_6$, with R1 = (0 4 4) and R2 = $(5\,\overline{2}\,\overline{1})$. Moreover, it possesses a crystal zone axis of $[1\,5\,\overline{5}]$. In Fig. 9(e), a micrograph captured by high-resolution transmission electron microscope is presented, accompanied by selected area diffraction pattern obtained through Fourier transform, as depicted in Fig. 9(f). This phase has been identified as $Cr_5B_3$ with $R1 = (\overline{1}\,0\,1)$, R2 = (1 1 0) and a crystal zone axis of $[1\,\overline{1}\,1]$. When integrating these findings with the

results of the energy spectroscopy tests, it is deduced that the long strip region in the figure corresponds to $Cr_5B_3$, while the block area corresponds to $Cr_{23}C_6$. Figure 8(g) illustrates the polycrystalline diffraction ring pattern acquired through selected area diffraction. The interplanar spacing related to the distinct diffraction rings of the precipitation phase can be calculated. The diffraction rings shown in Fig. 9(g) have been calibrated to correspond with $d1 = 2.072$ nm, $d2 = 1.799$ nm and $d3 = 1.441$ nm. Subsequently, the crystal face depicted in the diffraction ring display in Fig. 8(g) seems to correspond with (5 1 1) 2.052 nm, (5 3 1) 1.801 nm and (6 4 0) 1.478 nm of $Cr_{23}C_6$, according to the standard PDF diffraction cards. The diffraction rings in Fig. 8(h) precisely match the crystal face (0 0 4) with a value of 2.528 nm, (2 1 3) with a value of 1.981 nm and 1.809 nm (2 2 2) of $Cr_5B_3$, as identified in the standard diffraction card. Consequently, these results affirm the presence of $Cr_{23}C_6$ and $Cr_5B_3$ phases in the precipitated phase of the composite coatings.

**Fig. 9** (a, b) Morphology of precipitated phase in coating 3#; (c-f) high-resolution image and Fourier transform of precipitated phases; (g, h) SAED pattern of precipitated phases
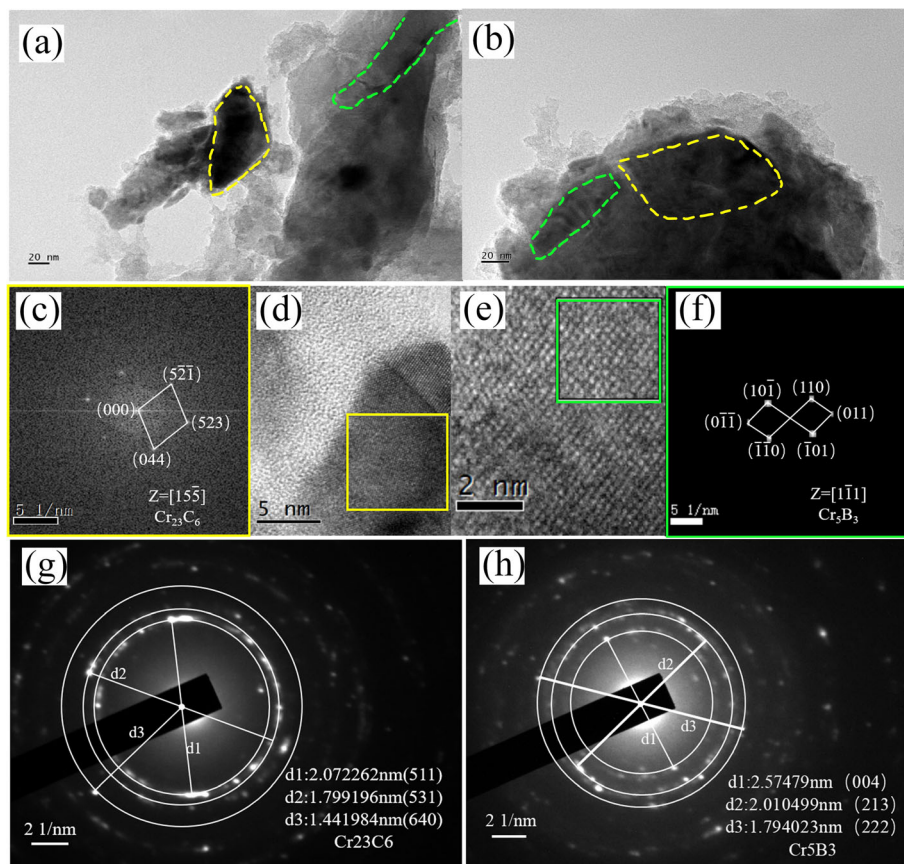


Based on our analysis of the experimental results, we have observed that the introduction of silicon (Si) into borides induces significant changes in crystal chemical bonding, crystal structure and growth behavior. XRD analysis reveals the transformation of Cr5B3 into (Cr, W)5(Si, B)3. The incorporation of Si fosters the formation of Cr-Si covalent bonds, partially displacing the previous Cr-B ionic bonds (Ref 38-40). This substitution enhances the anisotropy of the crystals, facilitating more directional growth in space during nucleation and nucleus growth in solidification. Consequently, the structure undergoes a transition from a homogeneous square shape to an elongated one.

## Microhardness and Wear Resistance

Figure 10(a) presents the microhardness distribution of the cladding with varying Si additions. The Q550 steel matrix maintains a microhardness of approximately 240 HV, with a significant and abrupt increase in microhardness observed at the interface of the cladding layers. The microhardness within the composite coating area is approximately three times higher than that of the matrix. Notably, the microhardness distribution in the cross section of the cladding layer exhibits certain fluctuations. Microstructure analysis

reveals an inhomogeneous distribution of in-situ precipitation phases in the composite coatings with varying Si additions. Additionally, the presence of a small quantity of unfused WC particles contributes to fluctuations in the microhardness of the cladding layer (Ref 41, 42). The microhardness results for different composite coatings are illustrated in Fig. 10(b). The average microhardness of the cladding layer exhibited an increase, while the size of microhardness indentation decreased gradually with the incremental addition of Si. In the control group, devoid of Si addition, the average microhardness of the cladding layer reached 769.8 HV, whereas in the test group with a 6 wt.% Si addition, the average microhardness escalated to 1016.8 HV. The substantial increase in microhardness in the composite coating is attributed to the addition of Si elements, primarily due to their involvement in the in-situ precipitation reaction within the cladding layer. This process promotes an increase in nucleation density and the formation of needle-like in-situ reinforced phase. The resulting $(Cr, W)_5(Si, B)_3$ precipitation phases exhibit a high level of microhardness and contribute to the overall increase in the average microhardness of the cladding layer (Ref 43-45).

The pin-on-disk testing was employed to evaluate the wear performance of various cladding layers, and the
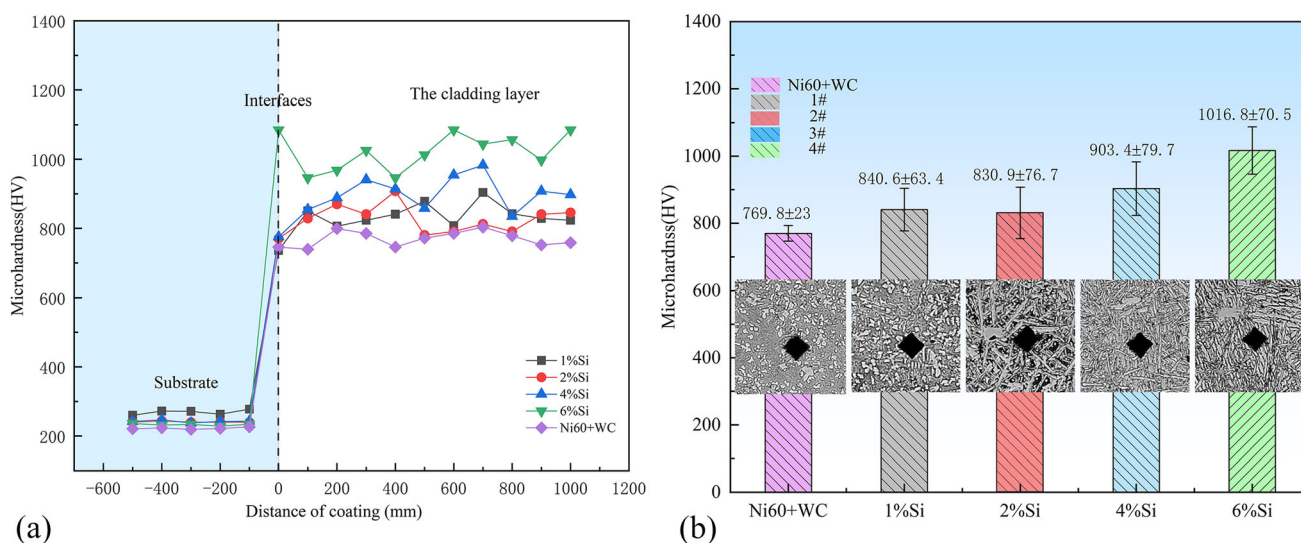
**Fig. 10** (a) Microhardness distribution of different coatings. (b) Average microhardness of different coatings
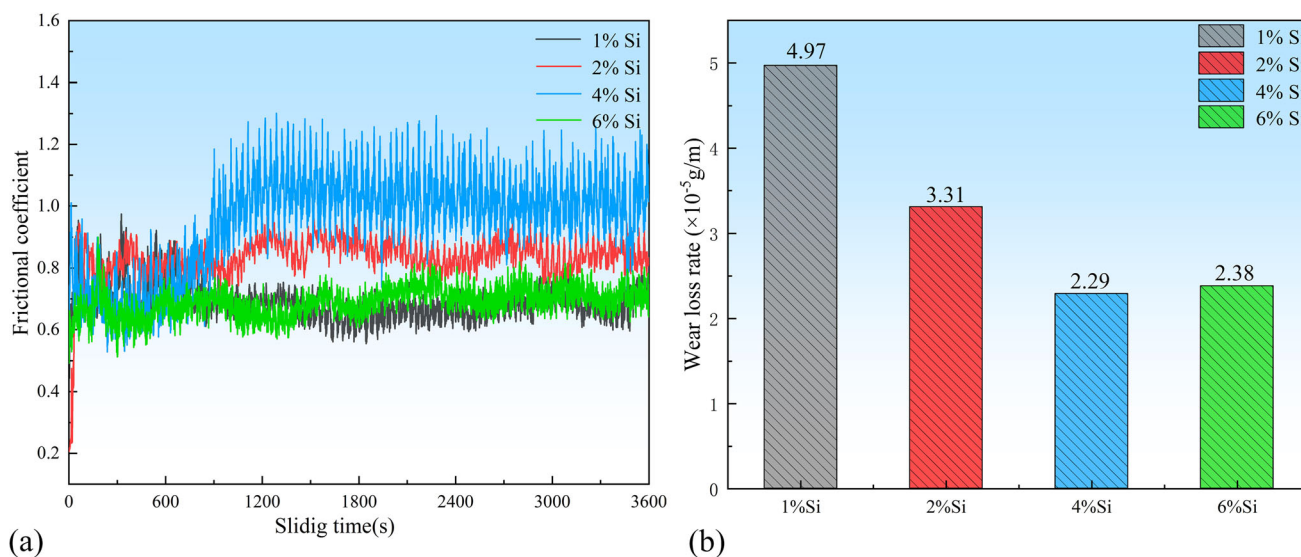


**Fig. 11** Results of pin-on-disk wear tests of different cladding layers. (a) Friction coefficient. (b) Wear weight loss

results are presented in Fig. 11. Figure 11(a) depicts the friction coefficient curves of the composite coatings with different Si additions. Notably, the cladding layer with 4 wt.% Si addition exhibits the highest friction coefficient, averaging around 1.1. The friction coefficient of the composite coating fluctuates around 0.9 with the 2 wt.% Si content, while it remains relatively low, ranging between 0.6 and 0.7, for cladding layers containing 1 and 6 wt.% of silicon. Figure 11(b) illustrates the wear loss rate of the composite coatings, revealing a gradual decrease with increasing Si content. The wear loss rate peaks of cladding layer with 1 wt.% Si addition at $4.97 \times 10^{-5}$ g/m. However, with the addition of 2 wt.% Si, the wear rate

decreases to $3.31 \times 10^{-5}$ g/m. The wear loss rates for cladding layers with 4 and 6 wt.% Si additions are relatively low, standing at $2.29 \times 10^{-5}$ g/m and $2.38 \times 10^{-5}$ g/m, respectively. Upon analyzing the microstructure and microhardness data of the composite coatings, the primary factor contributing to the enhanced microhardness of the cladding layer is attributed to the notably uniform distribution of dense and numerous precipitated phases. Consequently, the cladding layer exhibits a low coefficient of friction and wear loss under the applied load. Through comprehensive analysis, it can be concluded that the coating 4# demonstrates optimal comprehensive mechanical properties.

## Worn Surface Morphology and Mechanism

Figure 12 illustrates the worn surface characteristics of cladding layers with varying Si contents. In metal-based cladding layers reinforced with ceramic particles, wear failure predominantly manifests as abrasive and adhesive wear. The worn surface of the coating 1# exhibits an increased occurrence of spalling pits with diverse sizes and deeper in Fig. 12(a1). In Fig. 12(a2), a rise in abrasive debris is noticeable within the spalling pits. Upon conducting a microstructure analysis of the coating 1#, it was observed that the addition of 1 wt.% Si resulted in the form of many massive precipitated phases. These substantial precipitation phases are peeled off under heavy wear loads,

giving rise to a significant area of spalling pits. Following the shedding of the substantial precipitated phase which undergoes fragmentation into numerous fine hard phase particles, thereby intensifying abrasive wear on the surface. Figure 12(b1) and (b2) showcases the worn surface morphology with the inclusion of 2 wt.% Si in the composite coatings. The results indicate that the worn surface continues to exhibit a greater number of spalling pits, containing an increased quantity of fine hard phase particles. The microstructure of the coating 2# is subject to significant changes compared to the coating 1#, particularly in the morphology of the precipitated phase. The reduction in the size of the long strip precipitated phase tends to decrease the formation of spalling pits on the worn surface of



Fig. 12 Worn surface morphology of different cladding layers (a1, a2) coating 1#; (b1, b2) coating 2#; (c1, c2) coating 3#; (d1, d2) coating4#
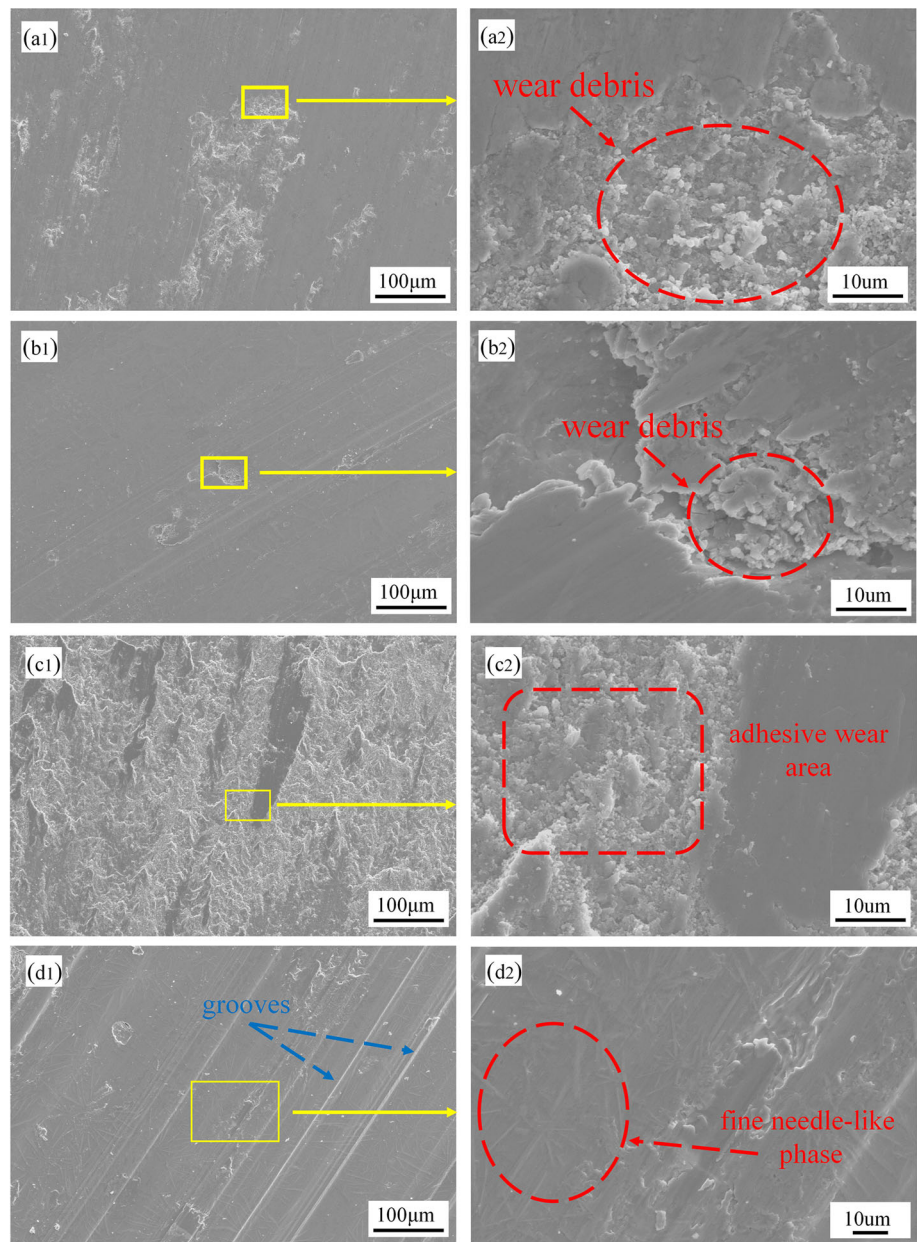
coating 2#, in contrast to the block precipitated phases. The elongated precipitated phase is further crushed and broken up after shedding, causing abrasive particles to appear on the previously clean wear surface. Furthermore, the volume of the elongated precipitated phase is smaller than that of the bulk precipitated phase, resulting in a reduction of abrasive particles on the wear surface and subsequently decreasing wear weight loss.

The quantity of hard phase particles formed is lower compared to that was observed in coating 1#. In Fig. 12(c1), the worn surface of the 4 wt.% Si cladding shows noticeable roughness, with multiple adherent wear areas and more spalling pits. Figure 12(c2) further illustrates these spalling pits containing a substantial amount of wear particles. With an increase in the Si element, the precipitated phase size of the cladding layer becomes finer. However, the average microhardness of the composite coating basically remains consistent. There is a decrease in the overall wear resistance of the cladding layer, potentially leading to significant adhesive wear on the surface. This results in a considerable rise in the coefficient of friction for the coating 3#. Figure 12(d1) and (d2) demonstrates that the addition of 6 wt.% Si cladding layer significantly reduces both the number and area distribution of spalling pits on the worn surface. Furthermore, the worn surface only exhibits a few grooves. The needle-like precipitated phases are uniformly embedded within the matrix and are observable in the un-peeled off rea of the worn surface in Fig. 12(d2). The close integration between these needle-like precipitated phases and the matrix is clearly evident from this observation. Moreover, the average microhardness of the coating 4# has been substantially enhanced compared to the other three composite coatings, displaying well resistance to wear without adhesive wear area. This leads to a reduction in the coefficient of friction, thereby improving the wear resistance. Following the peeling off the needle-like precipitation phase forms a limited number of small and hard phase particles. As a result, the diminished entry of abrasive particles into the opposing abrasive surface area of the flaking pit leads to a decrease in abrasive wear. The relatively low of wear debris into the worn surface of the spalling pits mitigates the abrasive wear.

By integrating microstructural analysis with an examination of the wear properties of the cladding and the worn surface morphology, this study delves into the worn surface mechanism of the cladding layers. Figure 13 explains how the wear mechanism varied when the morphology of the precipitated phases changes. The wear mechanism analyses are qualitative discussions aimed at providing possible explanations. In Fig. 13(a) and (b), a schematic diagram illustrates the wearing mechanism of the composite coating, reinforced by block precipitated phases under low Si addition. When subjected to wear load, the prominent block precipitated phases fractured at the interface, giving rise to spalling pits characterized by significant area and depth. The fragmentation of these block precipitated phases produces more wear debris which adheres to the worn surface, thus increasing abrasive wear while leading to reduced wear resistance.

Upon an increase in Si element content, the morphology of the precipitated phase within the composite claddings transformed from the block to the strip/needle-like microstructure. The ensuing discussion investigates the wear mechanism of this distinct strip/needle-like precipitated phase in the coating 4#, detailed in Fig. 13(c) and (d). Microstructural analysis reveals an absence of notable regularity in the directional arrangement of the strip/needle-like precipitated phases, therefore investigating the precipitated phases in two representative distribution directions. When the strip/needle-like precipitated phases project from the upper surface at a specific inclined angle, the lower sections of the precipitated phases intimately bond with the matrix, inducing mutual constraint and forming a pinning effect. Under the imposed wear load, only a minor portion of the upper precipitated phase fractures results in shallow spalling pits and a reduced generation of wear debris. This gradual and deep wear loss effect ensues. In instances where the precipitated phases align nearly parallel to the upper surface, the strip/needle-shaped precipitated phases exhibit a remarkably high aspect ratio which measured only about 3-5 μm radially. Even if the entire precipitated phase breaks due to wear load, the resulting formation of spalling pits remains shallow. Moreover, owing to the reduction in volume and quantity of reinforced phases, the generation of wear debris subsequent to fracture is diminished. Consequently, this enhances the wear resistance of the composite coating 4#.

## Conclusions

In this work, nickel-based composite coatings with good fusion effect and high wear resistance were produced by wide-band laser cladding technology. Based on microstructure analysis and characterization, and wear resistance testing, the following conclusions can be drawn:

(1) Microstructure analysis revealed that the shape of the precipitated phase in the cladding layer changes from massive to strip/needle-like as the Si element content increases. Moreover, the size of the precipitated phase decreases significantly, while the nucleation density increases.

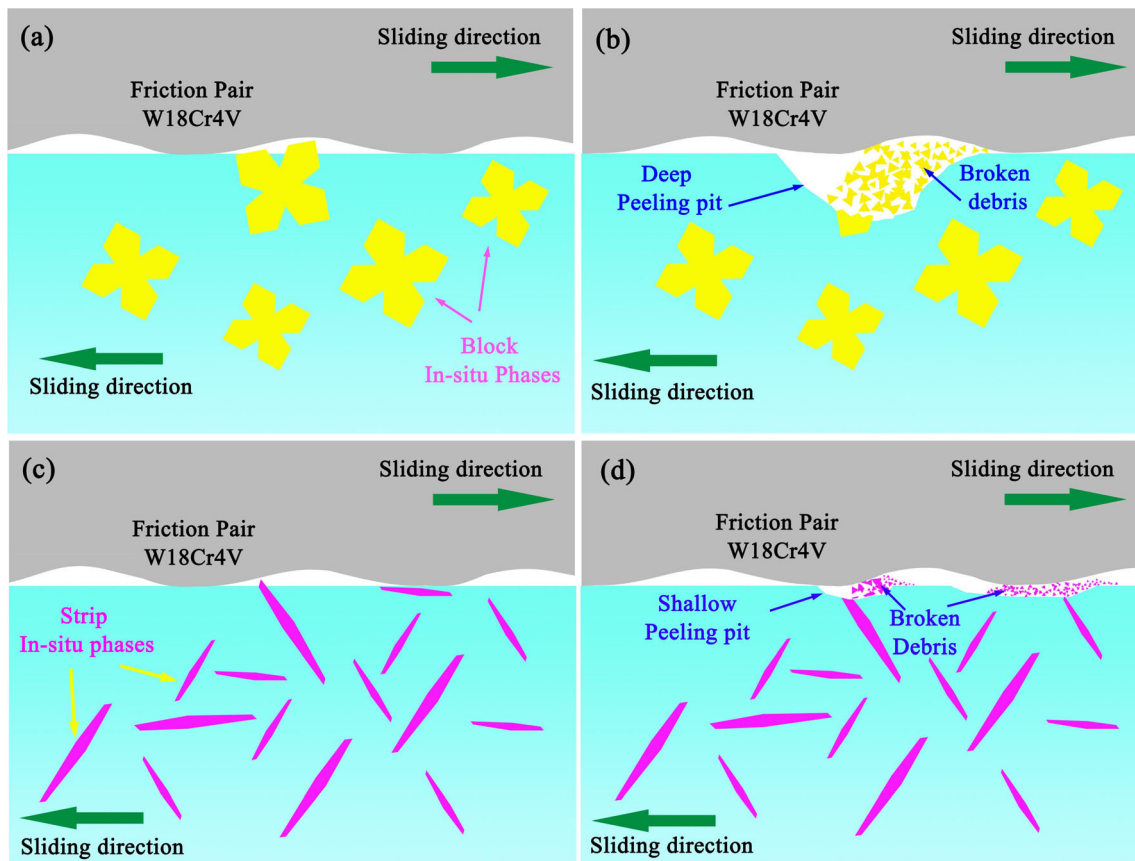(2) The phase of wide-band laser cladding composite coatings incorporating Si, enhanced by in-situ

**Fig. 13** Schematic diagram of the wear mechanism for different cladding layers (a, b) coating 1#; (c, d) coating 4#

precipitation, is primarily comprised of γ-Ni, $Cr_7C_3$, $Cr_{23}C_6$, $Cr_5B_3$ and CrSi. The phases formed through in-situ precipitation in the coating layers exhibit microstructures of the $A_5B_3$ type $(Cr, W)_5(Si, B)_3$ and manifest as both block and needle-like morphologies. Elemental analysis indicates a significant bias towards the Si element in the precipitated phases, suggesting heavy involvement of the added Si element in the in-situ reaction of the precipitated phases within the composite coatings.

(3) The alloying effect of Si element can significantly improve the microhardness and wear resistance of the cladding layers. The designed coating with 6 wt.% Si exhibited the best wear resistance in the experimental group. These results were due to the tightly bonded, refined needle-like precipitated phase with the matrix phase. The average microhardness of the cladding layer reached 1016.8 HV, the friction coefficient was approximately 0.6, and the weight loss rate of abrasion was only $2.38 \times 10^{-5}$ g/m.

## References

1. A. Pascu, J.M. Rosca, and E.M. Stanciu, Laser Cladding: From Experimental Research to Industrial Applications, *Mater. Today: Proc.*, 2019, **19**, p 1059-1065.
2. S. Li, K. Huang, Z. Zhang et al., Wear Mechanisms and Micro-Evaluation of WC + TiC Particle-reinforced Ni-based Composite Coatings Fabricated by Laser Cladding, *Mater CharactCharact*, 2023, **197**, 112699.
3. K. Qi and L. Jiang, Effect of Y2O3 on the Microstructures and Properties of Magnetic Field-Assisted Laser-Clad Co-Based Alloys, *J. Mater. Eng. Perform.*, 2023 https://doi.org/10.1007/s11665-023-08670-2
4. Z.U. Arif, M.Y. Khalid, E. Ur Rehman et al., A Review on Laser Cladding of High-entropy Alloys, Their Recent Trends and Potential Applications, *J. Manuf. Process.*, 2021, **68**, p 225-273.
5. C.K. Kim, S.G. Choi, J.H. Kim et al., Characterization of Surface Modification by Laser Cladding Using Low Melting Point Metal, *J. Ind. Eng. Chem.*, 2020, **87**, p 54-59.
6. C. Liu, P. Xu, D. Zheng et al., Study on Microstructure and Properties of a Fe-based SMA/PZT Composite Coating Produced by Laser Cladding, *J. Alloy. Compd.*, 2020, **831**, 154813.

7. S. Zhao, S. Xu, L. Yang et al., WC-Fe Metal-matrix Composite Coatings Fabricated by Laser Wire Cladding, *J. Mater. Process. Technol.*, 2022, **301**, 117438.

8. S. Cao, J. Liang, and J. Zhou, Evolution in Microstructure Features and Properties of Mo-containing Fe-Cr-Ni-B-Si Composite Coatings by Laser Cladding, *Mater CharactCharact*, 2022, **188**, 111926.

9. S. Liu, M. Pang, and F. Ji, Tribological Properties of Laser Cladding Nickel-based WC Reinforced Ag Self-lubricating Coating on RuT450 Surface, *Opt. Laser Technol.*, 2023, **163**, 109393.

10. L.L. Zhai, C.Y. Ban, and J.W. Zhang, Investigation on Laser Cladding Ni-Base Coating Assisted by Electromagnetic Field, *Opt. Laser Technol.*, 2019, **114**, p 81-88.

11. J. Wang, X. Cui, Y. Zhao et al., Microstructure and Performance Enhancement of the TiN/Fe-based Cladding Layer Induced by Mechanical Vibration Assisted Underwater Wet Laser Cladding, *Surf. Coat. Technol.*, 2024, **476**, 130176.

12. B. Wu, P. Dong, W. Yu et al., Effect of Laser Energy Density on Amorphous Phase Content and Properties of Fe-Based Amorphous Coatings, *J. Ther. Spray Technol*, 2023, **33**(1), p 221-232.

13. W. Wang, L.-Y. Lou, K.-C. Liu et al., Structure and Oxidation Behavior of a Chromium Coating on Zr Alloy Cladding Tubes Deposited by High-Speed Laser Cladding, *J. Ther. Spray Technol.*, 2023, **33**(1), p 246-259.

14. Y. Wang, L. Chai, F. Zhang et al., Laser-clad Al-Ti-Zr and Cr-Ti-Zr Coatings on Zr Alloy: Composition-induced Microstructural and Hardness Differences, *Int. J. Refract Metal Hard Mater.*, 2022, **109**, 105956.

15. G. Cui, X. Feng, W. Han et al., Microstructure and High Temperature Wear Behavior of In-Situ Synthesized Carbides Reinforced Mo-based Coating by Laser Cladding, *Surf. Coat. Technol.*, 2023, **467**, 129713.

16. Y. Zhao, T. Yu, J. Sun et al., Microstructure and Properties of Laser Cladded B4C/TiC/Ni-based Composite Coating, *Int. J. Refract Metal Hard Mater.*, 2020, **86**, p 1017-1030.

17. Q. Cai, G. Li, B. Wu et al., Effect of TiC Content on Microstructure and Properties of TiC/Ni60 Coatings on Ti6Al4V Alloy Deposited by Laser Cladding, *Opt. Laser Technol.*, 2024, **168**, 109854.

18. Z. Hu, Y. Li, B. Lu et al., Effect of WC Content on Microstructure and Properties of High-speed Laser Cladding Ni-based Coating, *Opt. Laser Technol.*, 2022, **155**, 108449.

19. Q. Wang, Q. Li, L. Zhang et al., Microstructure and Properties of Ni-WC Gradient Composite Coating Prepared by Laser Cladding, *Ceram. Int.*, 2022, **48**(6), p 7905-7917.

20. X. He, R.G. Song, and D.J. Kong, Microstructures and Properties of Ni/TiC/La2O3 Reinforced Al Based Composite Coatings by Laser Cladding, *Opt. Laser Technol.*, 2019, **117**, p 18-27.

21. D. Hu, Y. Liu, H. Chen et al., Microstructure and Properties of Ta-Reinforced NiCuBSi + WC Composite Coating Deposited on 5Cr5MoSiV1 Steel Substrate by Laser Cladding, *Opt. Laser Technol.*, 2021, **142**, 107210.

22. M. Qunshuang, L. Yajiang, and W. Juan, Effects of Ti Addition on Microstructure Homogenization and Wear Resistance of Wide-band Laser Clad Ni60/WC Composite Coatings, *Int. J. Refract Metal Hard Mater.*, 2017, **64**, p 225-233.

23. G. Jie, S. Yan, W. Kangning et al., Effect of Fe Content on Microstructure and Corrosion Resistance of Ni-based Alloy Formed by Laser Cladding, *Surf. Coat. Technol.*, 2022, **446**, 128761.

24. J. Li, X. Cui, Y. Guan et al., Effects of Cr Content on Microstructure and Tribological Properties of Laser Cladding Ti-based Coatings, *Tribol. Int.. Int.*, 2023, **187**, 108744.

25. S. Hong, Q. Ma, G. Liu et al., In-Situ Reinforced Phase Evolution and Wear Resistance of Nickel-based Composite Coatings Fabricated by Wide-band Laser Cladding with Nb Addition, *Opt. Laser Technol.*, 2023, **157**, 108678.

26. C.J. Liang, C.L. Wang, K.X. Zhang et al., Nucleation and Strengthening Mechanism of Laser Cladding Aluminum Alloy by Ni-Cr-B-Si Alloy Powder Based on Rare Earth Control, *J. Mater. Process. Technol.*, 2021, **294**, 117145.

27. W. Li, W. Liu, Z. Liu et al., Effect of CNT Content on the Microstructure and Friction Characteristics of DED-fabricated CNTs-Ni60/WC Coatings, *Surf. Coat. Technol.*, 2023, **473**, 129938.

28. Q. Yuan, L. Chai, T. Yang et al., Laser-clad FeCrAl/TiC Composite Coating on Ferrite/Martensitic Steel: Significant Grain Refinement and Wear Resistance Enhancement Induced by Adding TiC, *Surf. Coat. Technol.*, 2023, **456**, 129272.

29. J. Ning, Q. Lan, L. Zhu et al., Microstructure and Mechanical Properties of SiC-reinforced Inconel 718 Composites Fabricated by Laser Cladding, *Surf. Coat. Technol.*, 2023, **463**, 129514.

30. S. Singh, D.K. Goyal, P. Kumar et al., Influence of Laser Cladding Parameters on Slurry Erosion Performance of NiCrSiBC + 50WC Claddings, *Int. J. Refract Metal Hard Mater.*, 2022, **105**, 105825.

31. J. Liang, Y. Liu, S. Yang et al., Microstructure and Wear Resistance of Laser Cladding Ti-Al-Ni-Si Composite Coatings, *Surf. Coat. Technol.*, 2022, **445**, 128727.

32. Z.-X. Zhu, X.-B. Liu, Y.-F. Liu et al., Effects of Cu/Si on the Microstructure and Tribological Properties of FeCoCrNi High Entropy Alloy Coating by Laser Cladding, *Wear*, 2023, **512-513**, 204533.

33. W.-J. Dan, R.-B. Gou, M. Yu et al., Experimental Study on the Post-fire Mechanical Behaviours of Structural Steels, *J. Construct. Steel. Res.*, 2022, **199**, 107629.

34. Q. Ma, Y. Li, J. Wang et al., Investigation on Cored-eutectic Structure in Ni60/WC Composite Coatings Fabricated by Wide-band Laser Cladding, *J. Alloy. Compd.*, 2015, **645**, p 151-157.

35. H. Liu, S. Sun, T. Zhang et al., Effect of Si Addition on Microstructure and Wear Behavior of AlCoCrFeNi High-entropy Alloy Coatings Prepared by Laser Cladding, *Surf. Coat. Technol.*, 2021, **405**, 126522.

36. C. Chen, A. Feng, Y. Wei et al., Role of Nano WC Particles ADDITION on the Corrosion Behavior of Laser Cladding WC/Ni Coatings, *Mater. Lett.*, 2023, **337**, 133939.

37. J.M.S.D. Sousa, F. Ratusznei, M. Pereira et al., Abrasion Resistance of Ni-Cr-B-Si Coating Deposited by Laser Cladding Process, *Tribol. Int.. Int.*, 2020, **143**, 106002.

38. Y. Liu, H. Fu, W. Li et al., Mechanical Properties and Chemical Bonding of M2B and M2B0.75C0.25 (M = Fe, Cr, W, Mo, Mn) Compounds, *J. Mater. Res.*, 2018, **33**(22), p 1-12.

39. X. Lei, Y. Li, and X. Du, Morphological Features of Unmodified Eutectic Si and Morphological Transformation after Solution Treatment, *Mater. Lett.*, 2024, **358**, 135870.

40. X. Jin, V. Arcisauskaite, and J.E. McGrady, Quantum Chemical Models for the Absorption of Endohedral Clusters on Si (111)-(7× 7): a subtle Balance Between W-Si and Si-Si Bonding [J], *Phys. Chem. Chem. Phys.*, 2019, **21**(25), p 13686-13695.

41. G.-D. Chen, X.-B. Liu, F.-Z. Zhang et al., Fabrication and Tribological Properties of Laser Cladding WC-Cu/Co-based Composite Coatings, *Surf. Coat. Technol.*, 2023, **472**, 129930.

42. S. Singh, A. Bansal, P. Kumar et al., Slurry Erosion Behavior of HOGONAS+50%WC Cladded SS304 Steel Prepared Using Variable Laser Cladding Parameters, *Int. J. Refract Metal Hard Mater.*, 2023, **115**, 106326.

43. X. Chen, X. Qin, Z. Zhu et al., Microstructural Evolution and Wear Properties of the Continual Local Induction Cladding NiCrBSi Coatings, *J. Mater. Process. Technol.*, 2018, **262**, p 257-268.

44. X. Luo, J. Li, and G. Li, Effect of NiCrBSi Content on Microstructural Evolution, Cracking Susceptibility and Wear Behaviors of Laser Cladding WC/Ni-NiCrBSi Composite Coatings, *J. Alloy. Compd.*, 2015, **626**, p 102-111.

45. Z. Shengfeng, J. Lei et al., A Comparative Study of the Structure and Wear Resistance of NiCrBSi/50 wt.% WC Composite Coatings by Laser Cladding and Laser Induction Hybrid Cladding, *Int. J. Refract. Metals Hard Mater.*, 2016, **60**, p 17-27.